

# Antireflection subwavelength structures on fused silica fabricated by colloidal microsphere lithography

X. YE<sup>a</sup>, J. HUANG<sup>a</sup>, B. LI<sup>a,b</sup>, F. GENG<sup>a</sup>, H. J. LIU<sup>a</sup>, F. R. WANG<sup>a</sup>, X. D. JIANG<sup>a\*</sup>, W. D. WU<sup>a</sup>, W. G. ZHENG<sup>a,c</sup>

<sup>a</sup>Research Center of Laser Fusion, China Academy of Engineering Physics, Mianyang 621900, China

<sup>b</sup>Joint Laboratory for Extreme Conditions Matter Properties, Southwest University of Science and Technology and Research Center of Laser Fusion, CAEP, Mianyang 621900, CHINA

<sup>c</sup>IFSA Collaborative Innovation center, Shanghai jiao tong University, Shanghai, 200240, P.R. China

In this paper we present a simple method to fabricate ordered antireflection structures on a fused silica using reactive ion etching and monolayer colloidal microspheres lithography. We show that the period of the obtained silica pillar-like arrays were determined by the initial nanoparticle size. And the height of pillar arrays can be adjusted by controlling the etching time, which are proved to be of importance in tailoring the antireflection properties of antireflection structures surface. For the single side antireflection structures on the fused silica, the reflectance was significantly reduced below 3.5 % over a wide wavelength range of 300-1200nm, while the transmission was improve to 96 %. The structure which has frustum of cone profile exhibited excellent broadband antireflection properties and large angle view properties. However, the size of the antireflection structures affects the antireflective properties in short wavelength region.

(Received September 28, 2015; accepted October 28, 2015)

*Keywords:* Antireflection structures; Colloidal microsphere lithography; Reactive ion etching

## 1. Introduction

In recent years, steady efforts have been made to achieve broadband antireflection characteristics for various optical elements, [1-4] such as broadband and omnidirectional antireflection coatings [5], high-efficiency field emission devices [2], high-sensitivity sensors [1], and highly hydrophobic surfaces[6]. Some moths use arrays of nipples of subwavelength size as antireflective structures (ARS) to reduce reflection from their compound eyes [7, 8]. The ARS on the cornea of these insects can also increase light transmission in dark conditions, which improves the sensitivity of light vision. The ARS surface with a period shorter than the wavelengths of visible light can suppress the reflection of light. This antireflection effect provided by a microstructured surface is known as a “moth-eye”, and the ARS surface is called an antireflective sub-wavelength structures surface [9]. For the current anti-reflective technologies, thin film coatings deposited by multiplayer stack or sol-gel method have become the industry standard for antireflection coatings (ARCs) [10]. Unfortunately, these existing techniques often are expensive to implement, impeding development of optical application that can be made truly economically competitive with fossil fuels. Additional, when coatings using multilayer thin-film stacks are applied for antireflection, there still exist many problems associated with band limitation, material selection, thermal mismatch

between the film and the substrate[11]. The ARS surfaces possess distinct advantages compared to coatings. First, the ARS surfaces exhibit higher mechanical stability and better durability than coatings because no external materials are involved when they are used over a broad thermal range, especially in the infrared region[12]. Second, material of the ARS surfaces is the same as that of elements. In the field of infrared optics, refractive indices of optical materials are very high and proper materials for antireflective antireflective coatings based on multilayered films are rare in nature [13].

Top-down technologies, such as interference lithography[14], electron beam lithography[15, 16] and photolithography[17] are commonly used to generate sub-wavelength structures ARCs. Such a feature size is beyond the conventional photolithography capability. Deep-ultraviolet photolithography can have feature sizes as small as 90 nm, but it requires expensive facilities. Electron beam lithography and fast atom beam etching have been used for creating nanoscale antireflection structuresd surfaces. However, these procedures are expensive and also very time consuming. Self-assembly technology provides a much simpler and cheaper alternative in creating sub-micrometer scale periodic arrays. Recently, ARS surfaces on silicon prepared by nanosphere lithography have been reported, but there are few works about ARS surfaces on silica were reported. And silica is an important material for many application

fields such as transparency optical system.

In this study, we demonstrate how silica nanopillar arrays with antireflective behavior are created based on the combination of self-assembly of polymer spheres into two dimensional (2D) arrays and reactive-ion etching (RIE).

## 2. Experimental procedure

A schematic diagram of process steps for fabricating the ARSs by colloidal crystals template and RIE on silica substrate is shown in Fig. 1. First, the gas-water self-assembly technique is firstly used to generate ncp colloidal monolayers of hexagonally ordered PS particles on silica wafers. Monodisperse PS particles with diameters of 260 nm were produced by an emulsifier-free emulsion polymerization synthesis. Before Self-assembly, PS particles were modified with Sodium dodecyl sulfate (SDS) so as to terminate them with negative charged groups and prevent aggregation. Second, Silica nanopillars were formed by fluorine based chemistry selective and anisotropic RIE of the silica substrate using a maxture of Ar, oxygen and  $\text{CHF}_3$ . PS particles protect silica immediately underneath them from being etched, resulting in the formation of nipple arrays directly on silica surface. The patterns of the polystyrene spheres were transferred to the silica substrates, the diameter and spacing of the nanopillars were determined by the initial nanoparticle size and both PS and silica etching times. Finally, the templating PS particles at the tips of pillars can be selectively removed by oxygen reactive ion etching to generate clean silica pillar arrays.

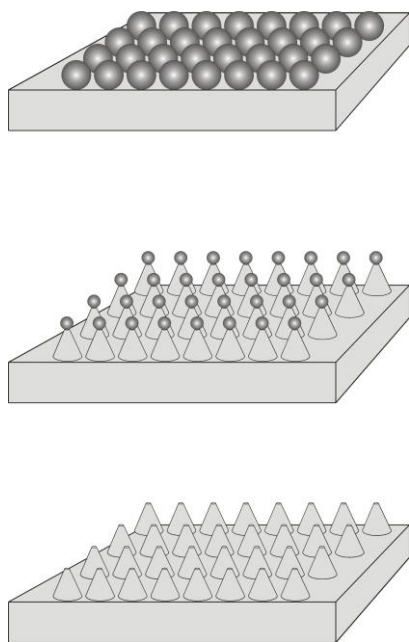


Fig. 1 Schematic of the fabrication procedures for the shape control of nanopillars. From the top, the schematics show a self-assembled PS particle monolayer, etching by fluorine based RIE, and post-cleaning process by Oxygen RIE process

### 2.1. Synthesis of monodisperse PS

Monodisperse PS was synthesized using an emulsifier-free emulsion polymerization technique. A five neck, round-bottomed flask was filled with water and the washed styrene, removed polymerization inhibitor, and then heated to 80 °C. Attached to the flask was an electric motor driving a glass string rod and Teflon wedge, a thermometer, a condenser, a pipe through which house nitrogen was bubbled to deaerate the mixture, and a stopper for the addition of reactants. Then the hot initiator solution (potassium persulfate) was added into the flask. The temperature was kept at 80°C while the mixed solution was stirred at about 300r/min for 24 hours. The resulting latex spheres remained suspended in their mother liquor until needed. The concentration can be adjusted by adding deionized water into the mother liquor.

### 2.2. Assembly of the 2D PS colloidal crystal templates

The fused silica substrates were cut into 20 mm \* 20 mm pieces, soaked in the mixture of 98%  $\text{H}_2\text{SO}_4$ / 30%  $\text{H}_2\text{O}_2$  (volumetric ratio 7:3) for 20 min under boiling (caution: strong oxide), and then rinsed with deionized water several times and dried with  $\text{N}_2$  stream. All the chemical reagents in our work were used as received. The PS microsphere monolayers were prepared by gas/water selfassembly. Experimental procedures of assembly the colloidal crystal are as follows: First, the deposition of a colloidal dispersion drop on the initial solid substrate, after drying of the dispersion, the particles are floated at the air/water interface by slow immersion of the parent substrate under a shallow angle. The PS particles detach from the substrate at the substrate-water-air three phase contact line, self-assemble in a dense monolayer, and remain afloat at the air/water interface. Subsequently, the floating layer of colloidal particles can be picked up by a second substrate. For that purpose the receiving substrate is immersed into the water and is slowly withdrawn at a shallow angle, just reverse to the immersion process. Finally the receiving substrate is kept at a fixed angle until all liquid is evaporated. The temperature for the experiment was set at  $20 \pm 2$  °C.

### 2.3 ARS Surfaces Fabricated by reactive ion etching (RIE).

The ARS surfaces were fabricated by RIE process. The RIE process was using a 20:2:1 mixture of Ar,  $\text{CHF}_3$  and  $\text{O}_2$  as a process gas at a total flow rate of 166 SCCM, chamber pressure 40 mTorr and RF power 100 W for appropriate time. Templating PS spheres are finally removed by oxygen RIE process for 30 min. Samples were washed with ethanol to generate clean silica nanopillar arrays.

## 2.4. Characterization

The diameter of the spheres was estimated using Mastersizer 2000 Laser particle sizer. The morphology of the colloidal crystals template and ARSs were examined using a JSM-7401 scanning electron microscopy (SEM) with primary electron energy of 5 kV. The samples were sputtered with a thin layer of Au prior to imaging. The wavelength-dependent reflectance and transmittance measurements for wavelengths between 300 nm and 1400 nm were measured using a PerkinElmer Lambda 950 UV-VIS-NIR spectrophotometer. The transmittance spectrum was measured at an incidence angle of 0–45°.

## 3. Results and discussion

### 3.1 2D PS colloidal crystal templates

During the fabrication of periodic particle arrays, to consolidate the particles, the water surface tension was changed by the addition of 4  $\mu\text{l}$  of 2 wt. % SDS and a large monolayer with highly ordered areas was obtained. Such monolayers were then lifted off from the water surface using previously mentioned silica wafers (Fig. 2 A). In the

process of array template formation, the general procedure for the colloidal monolayer formation involves first deposition and drying of a colloidal film from aqueous suspension on a parent substrate (top of Fig. 2 A). Upon immersion of the coated parent substrate into water, the particles float and pack into a dense, ordered monolayer at the air/water interface (mid of Fig. 2 A). From there the newly formed monolayer can be conveniently picked up by another substrate (bottom of Fig. 2 A).

From Fig. 2 B and C, we can see a typical structure of such prepared mask. The detailed organization of the spheres was investigated by scanning electron microscopy (SEM). Fig. 2B shows a top view SEM image of a monolayer colloidal crystal consisting of 260 nm diameter PS microsphere prepared by the gas-water interface self-assembly technology. The long-range hexagonal arrangement and the closed-pack structure of PS microsphere are evident. We can see that the packing structure of PS microspheres is face-centered cubic (fcc) with the (111) plane parallel to the surface of the substrate. Fig. 2C shows a tilt view SEM image of relatively large area of the self-assembled monolayer.

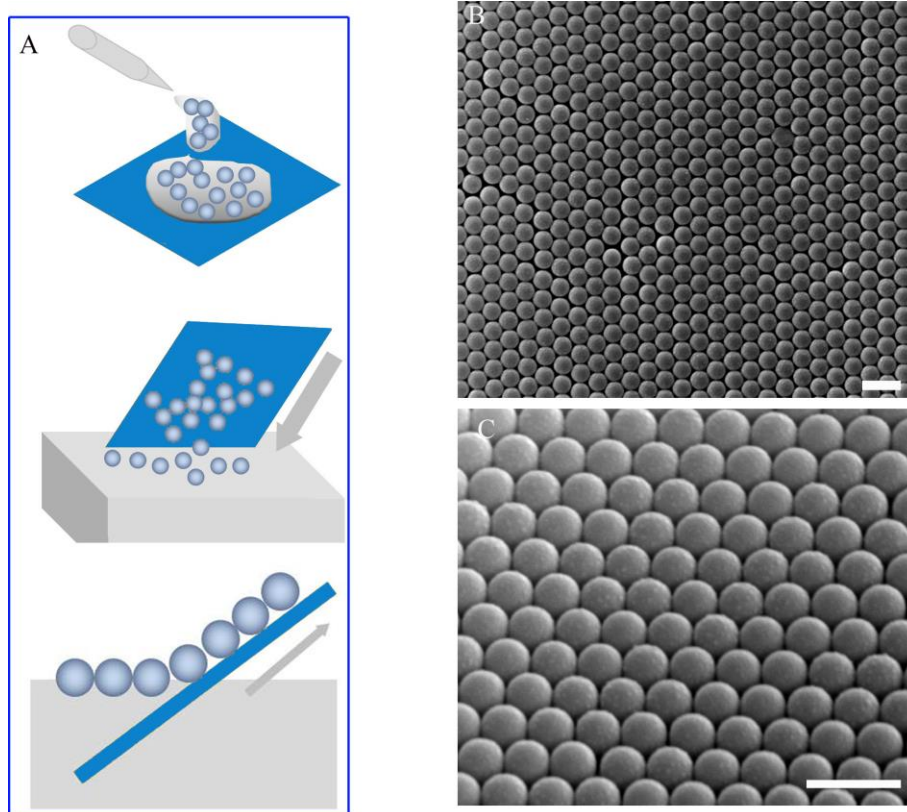


Fig. 2. (A) The preparation process of monolayer colloidal crystals masks: first, application of latex PS particles onto substrate surface; second, PS microsphere self-assembly on the gas/water interface; last, transfer monolayer colloidal crystals to silica substrate. (B) top view SEM of monolayer colloidal crystals; (C) tilt view SEM of monolayer colloidal crystals.

### 3.2 Morphology of ARSs

As shown in Figure 4A–F, pillar-like arrays were etched into the substrate by RIE. The fused silica substrate with the hexagonally non-close-packed nanopillar array was etched by the RIE process with Ar, oxygen and  $\text{CHF}_3$ . Fig. 4 B and E shows the nanopillar array with PS microsphere on the top of pillar. From these images, we can see that PS microsphere become non-sphere profiles. After the PS microspheres are completely removed by the last step Oxygen RIE process. The silica pillar arrays are obtained, as shown in Fig.4C and F. Obviously, the patterns of the masks can be accurately transferred onto the fused silica substrates using RIE, as the periodicity of the fused silica nanopillars array is consistent with that of the PS microspheres (Fig.4A,D). In our case, the height and shape of nanopillar can be controlled by varying the etching duration. The etching selectivity of PS to silica is about 1:20 which resulted in non-close-packed Silica nanopillar arrays. Subwavelength scale pillars with aspect

ratio as high as 5.0, can be easily fabricated by this approach. The Silica nanopillar arrays of different heights can be fabricated by adjusting the etching duration from 7 to 12mins. As presented in Figure 4C, the fused silica nanopillars with similar pillar to the mask spheres were fabricated using 7min etching, and are about 250nm in height. Upon extending the etching duration to 12 min, the height of the Silica nanopillars increased to 415 nm, and the shape of the Silica nanopillars changed from pillar to frustum of cone (see Fig. 4F). In the process of RIE, the PS microspheres act as masks, but they can also be etched by the reactive ions. During the etching, the diameter of the PS microspheres decreases, leading to the formation of truncated cone-shaped profiles(Fig. 4F). For PS microspheres monolayer mask, its edges are etched and eroded during the overall etching, thus leading to a nanobumps etching profile on lateral of nanopillars (Fig. 4E).

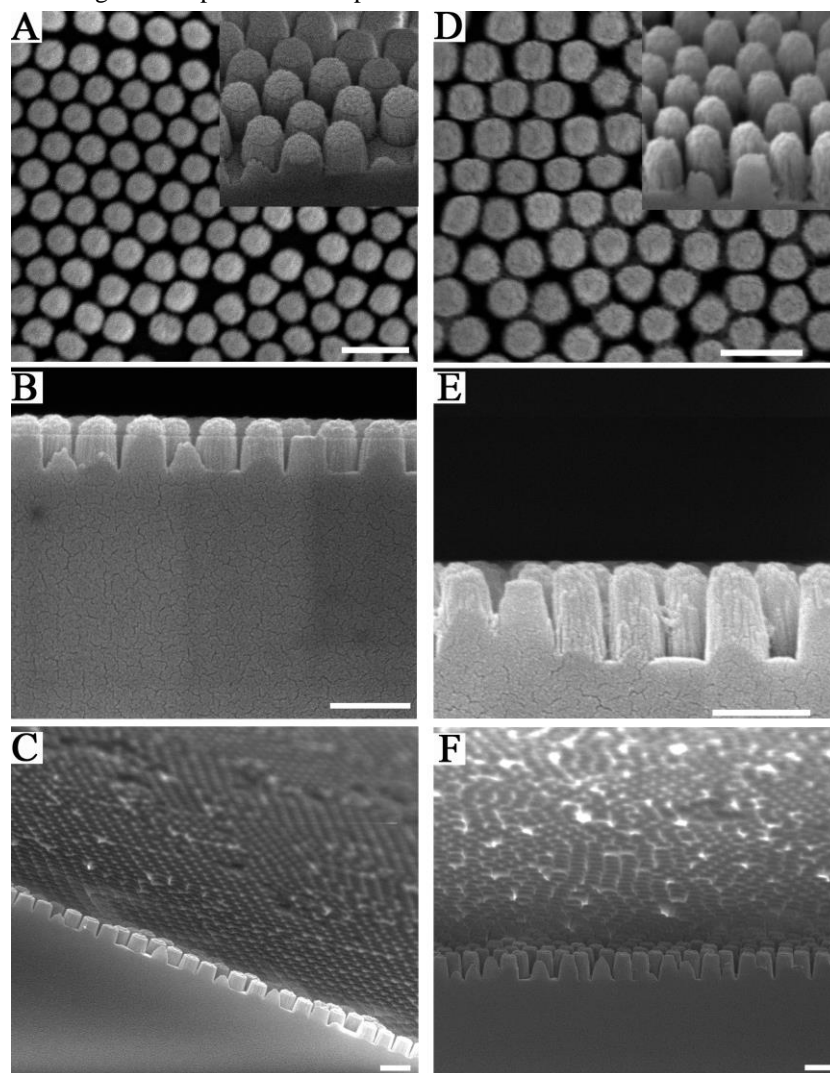


Fig. 4 (A,D) SEM image of the top view of the nanopillars array with PS particles mask, inset, tilted-view SEM image showing the pillar-like profiles. (B,E) Cross-sectional view SEM image of the nanopillars array with PS particles mask. (C,F) Removal of the residual mask by tetrahydrofuran etching. The durations of the reactive ion etching are (A,B,C) 7 min, (D,E,F) 12min.

### 3.3 Optical Properties of ARS

The ARS surfaces have similar morphologies with the nipple arrays on cornea of moth, which dramatically suppress the reflection loss and increase the transmittance of light. The optical performance of the ARS presented here was investigated by wavelength-dependent transmission and reflection measurements in the 300 nm - 1200 nm range. Transmission and reflection measurements were performed using a Lambda 950 spectrometer (The specular reflection were measured at an incidence angle of  $15^\circ$  and transmission were measured at a normal incidence.)

As shown in Figure 4 A, for the single-sided ARS surfaces with pillar-like arrays of 260 nm in period, and 415 nm in height, The ARS surfaces reduces the reflection at wavelengths from 300 to 1200 nm. The maximum transmittance from 1000 to 1200 nm is 96.5% (the red line in Figure 4A), while the transmission of planar silica substrate is ~93% (the black line in Fig. 4A). Fig. 4 C show that the reflectivity is ~3.5% from 300 to 1200nm, while improvement of reflectivity is less than the ~7% reflection of a normal fused silica surface reflectivity. The reflectivity of light was decreased while transmission increased at the same time from 450nm to 1200nm.

The angle-dependent ( $0^\circ$  to  $45^\circ$ ) specular transmission of the ARS is evaluated in the Experimental section by an ultraviolet-visible spectral measurement accessory (Lambda 950 spectrometer). Figure 4B shows the transmission spectra with the incident angles of  $0^\circ$ ,  $15^\circ$ ,  $30^\circ$ , and  $45^\circ$ . It shows that for the incident angle of  $0^\circ$ , the transmission of single-side ARS is >96% from 600 to 1200nm (the green line in Fig. 4B). The transmission still exhibits an average transmission as high as the case at normal incidence in the long wavelength region(>900nm), When the incident angles increase to  $15^\circ$  and  $30^\circ$  (the red line and blue line in Fig. 4B). However, the specular transmission of the ARS decreases increases with the incidence angle in the short wavelength region (450~900nm). However, when the incident angle is larger

than  $30^\circ$ , the transmission over the spectra range is rapidly decreased. The average transmission of single-side ARS is less than 95%, when the angle is up to  $45^\circ$  (the pink line in Fig. 4B). This is because the average refractive index profile from air to fused silica substrate changes considerably from the case at normal incidence.

Fig. 4D shows the sum of the reflectance and transmittance of the ARS surfaces. We verified that the addition of reflection and transmission of the interface is less than 100%, indicating light loss in the short wavelength region. Previously, some researchers have reported that the sum of the transmittance and reflectance of transparent ARS is not 100% in the short wavelength region. There, the size of the protuberances affects the antireflective properties. To create no scattering from these microstructures at any incidence angle, the period  $p$  should be deliver[18]:  $P < \lambda_{\min}/2n$ ,  $n$  is the refractive index of substrate. Therefore, the light scattering on the surface is the main reason for the sum of transmission and reflection less than 100% in short wavelength region. For ultraviolet light (351nm) applications, feature sizes below 120nm are always necessary.

Fig. 4E shows the transmission of nanopillar ARS arrays with different height which were etched by different time. Remarkably, as shown in Fig. 4 E, the transmission spectra reveal the maximum values of specific wavelengths in relation to the height of the nanopillars. The maximum transmission peaks in the spectra shift to the long wavelength range as the height of nanopillars increases. And the nanopillar arrays which was shown in Fig. 3 F exhibit excellent broadband antireflection because of truncated cone-shaped profiles (the green line in Fig. 4E). Figure 4F shows the single-sided ARS and planar silica substrate exposed to sunlight. The background below the single-sided ARS demonstrates high-quality transparency and little reflection loss (left), while the planar silica substrate reflects sunlight (right).

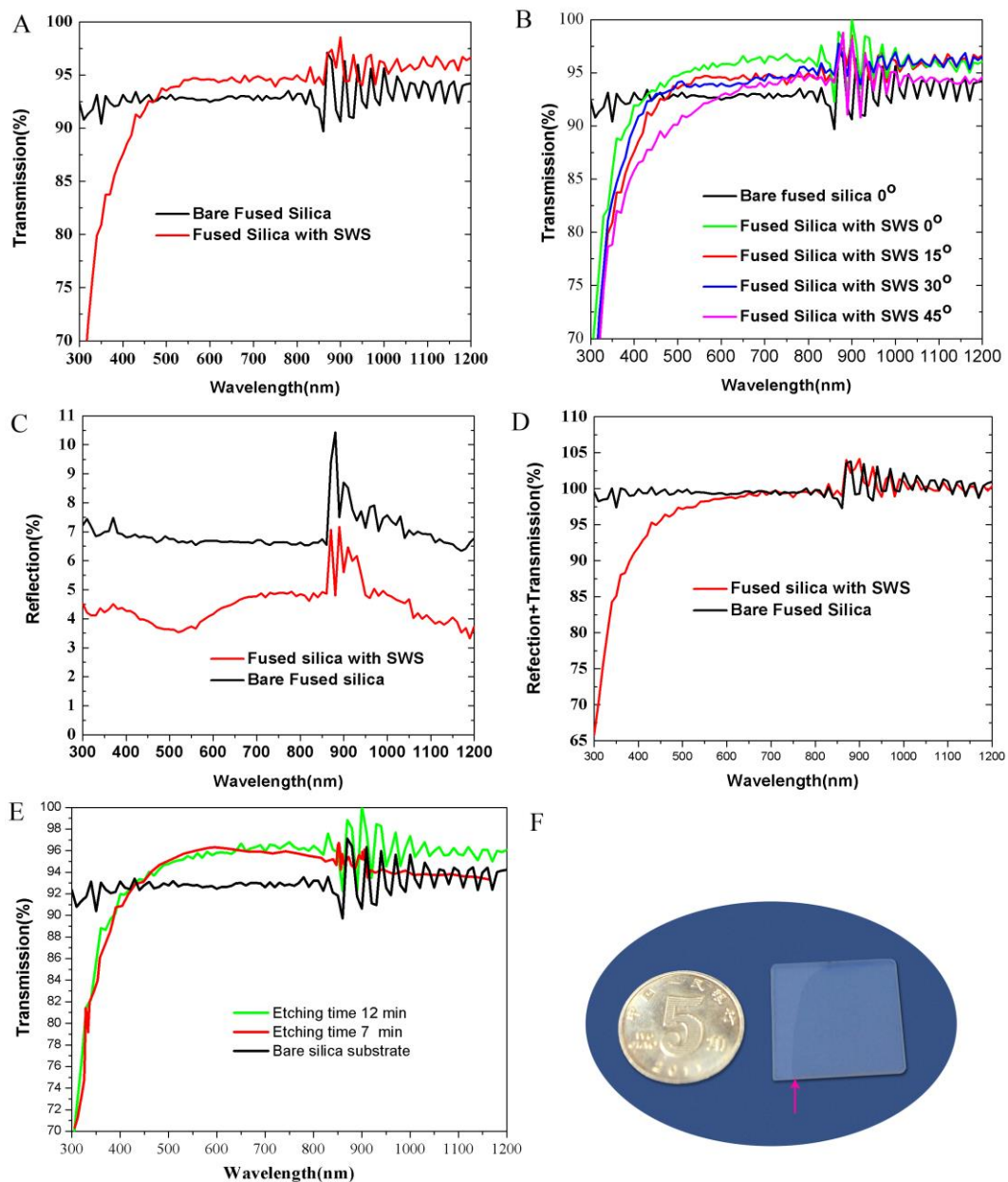


Fig. 4 High performance antireflective properties of the ARS surfaces. (A) Comparison of the specular transmission as a function of wavelength for a bare fused silica substrate (black line) and single-sided ARS (red line). (B) Wavelength and angle-dependent specular transmission of the single-sided ARS surfaces. (C) Wavelength dependent reflection of bare fused silica substrate (black line), single-sided ARS (red line). (D) The sum of measured transmittance and reflectance of the fabricated ARS surfaces with 260nm in heights. All spectra were measured with an incident angle of  $15^\circ$ . (E) The transmission for the fused silica ARS etched by different time in the wave band of 300–1200 nm. (F) Comparison of the photographs of fused silica substrate with single-sided ARS surfaces (right) and bare fused silica (left).

#### 4. Conclusion

In summary, we have demonstrated a simple colloidal microsphere lithographic technique for fabricating antireflective fused silica ARS arrays using self-assembled polystyrene sphere monolayers as etching masks. A smooth pillar-like array with a high aspect ratio was

fabricated upon a fused silica substrate. It was shown that the transmission of the single-side ARS had been increased to more than 96.5% while the reflectivity reduced to 0.5% at the same time. However, the size of the ARS affects the antireflective properties because of scattering. It should be possible to further decrease the scattering by optimizing the etching conditions and choosing proper spheres. This

method provides a simple approach for suppressing reflection over a large range of wavelengths and a large field of view on large areas with low cost and high throughput, and may have applications in high power laser fields to improve the laser induce damage threshold and optoelectronic fields.

### Acknowledgments

This work was supported by funds from State Key Laboratory of Ultra-Precision Machining Technology foundation of CAEP (ZZ13021, ZZ14010), the National Key Scientific Instrument and Equipment Development Project of China (No. 2014YQ090709), National Natural Science Foundation of China (No. 60908023), Science and Technology Development Foundation of Chinese Academy of Engineering Physics (No. 2010B0401055, 2013A0302016).

### Reference

- [1] H. Toyota, A. Mizutani, H. Kikuta, et al., in: *Physics, Theory, and Applications of Periodic Structures in Optics I*, P. Lalanne (Ed.), **5184**, 89 (2003).
- [2] Y. C. Kim and Y. R. Do, *Opt. Express* **13**,1598 (2005).
- [3] J. Sanghera, C. Florea, L. Busse, et al., *Opt. Express* **18**, 26760 (2010).
- [4] A. Asadollahbaik, S. A. Boden, M. D. Charlton, et al., *Opt Express* **22 Suppl 2**,A402 (2014).
- [5] X. Ye, J. Huang, J. C. Zhang, et al., *J. Optoelectron. Adv. Mater.* **13**,532 (2011).
- [6] X. Ye, J. Huang, R. F. Ni, et al., *J. Optoelectron. Adv. Mater.* **17**,192 (2015).
- [7] P. B. Clapham, M. C. Hutley, *Nature* **244**,281 (1973).
- [8] H. W. Deckman, J. H. Dunsmuir, *Appl. Phys. Lett.* **41**,377 (1982).
- [9] X. Ye, X. Jiang, J. Huang, et al., *Sci. Rep.* **5** (2015).
- [10] J. Q. Xi, M. F. Schubert, J. K. Kim, et al., *Nat. Photonics* **1**,176 (2007).
- [11] P. Karasinski, J. Jaglarz, M. Reben, et al., *Opt. Mater.* **33**,1989 (2011).
- [12] L. G. Xu, Z. Geng, J. H. He, et al., *ACS Appl. Mater. Interfaces* **6**,9029 (2014).
- [13] Y. F. Li, J. H. Zhang and B. Yang, *Nano Today* **5**,117 (2010).
- [14] K. C. Park, H. J. Choi, C. H. Chang, et al., *ACS nano* **6**,3789 (2012).
- [15] R. E. Smith, M. E. Warren, J. R. Wendt, et al., *Opt. Lett.* **21**,1201 (1996).
- [16] J. R. Wendt, G. A. Vawter, R. E. Smith, et al., *Journal of Vacuum Science & Technology B* **14**,4096 (1996).
- [17] J. Amako, D. Sawaki and E. Fujii, in: *Laser-Based Micro- and Nanopackaging and Assembly V*, W. Pfleging, Y. Lu, K. Washio, J. Amako, W. Hoving (Eds.), Vol. 7921. *Spie-Int Soc Optical Engineering*, Bellingham (2011).
- [18] M. Schulze, H. J. Fuchs, E. B. Kley, et al., in: *Advanced Fabrication Technologies for Micro/Nano Optics and Photonics*, T. J. Suleski, W. V. Schoenfeld and J. J. Wang (Eds.), Vol. 6883, pp. N8830. *Spie-Int Soc Optical Engineering*, Bellingham (2008).

---

\* Corresponding author: yehanwin@mail.ustc.edu.cn